

3-1-2008

A Tight-Binding Study of the Ballistic Injection Velocity for Ultrathin-Body SOI MOSFETs

Yang Liu

Purdue University - Main Campus

Neophytos Neophytou

Purdue University - Main Campus

Tony Low

Purdue University - Main Campus

Gerhard Klimeck

Purdue University - Main Campus, gekco@purdue.edu

Mark Lundstrom

Purdue University - Main Campus

Follow this and additional works at: <http://docs.lib.purdue.edu/nanodocs>

Liu, Yang; Neophytou, Neophytos; Low, Tony; Klimeck, Gerhard; and Lundstrom, Mark, "A Tight-Binding Study of the Ballistic Injection Velocity for Ultrathin-Body SOI MOSFETs" (2008). *Other Nanotechnology Publications*. Paper 73.
<http://docs.lib.purdue.edu/nanodocs/73>

This document has been made available through Purdue e-Pubs, a service of the Purdue University Libraries. Please contact epubs@purdue.edu for additional information.

A Tight-Binding Study of the Ballistic Injection Velocity for Ultrathin-Body SOI MOSFETs

Yang Liu, *Student Member, IEEE*, Neophytos Neophytou, *Student Member, IEEE*, Tony Low, *Student Member, IEEE*, Gerhard Klimeck, *Senior Member, IEEE*, and Mark S. Lundstrom, *Fellow, IEEE*

Abstract—This paper examines the validity of the widely used parabolic effective mass approximation by computing the ballistic injection velocity of a double-gate, ultrathin-body (UTB) n-MOSFET. The energy dispersion relations for a Si UTB are first computed by using a 20-band $sp^3 d^5 s^*$ -SO semiempirical atomistic tight-binding (TB) model coupled with a self-consistent Poisson solver. A semiclassical ballistic FET model is then used to evaluate the ballistic injection velocity of the n-type UTB MOSFET based on both an TB dispersion relation and parabolic energy bands. In comparison with the TB approach, the parabolic band model with bulk effective masses is found to be reasonably accurate as a first-order approximation until down to about 3 nm, where the ballistic injection velocity is significantly overestimated. Such significant nonparabolicity effects on ballistic injection velocity are observed for various surface/transport orientations. Meanwhile, the injection velocity shows strong dependence on the device structure as the thickness of the UTB changes. Finally, the injection velocity is found to have the same trend as mobility for different surface/transport orientations, indicating a correlation between them.

Index Terms—Band structure, effective mass, injection velocity, MOSFETs, nonparabolicity, pseudopotential (PP), quantum confinement, tight-binding (TB), ultrathin-body (UTB).

I. INTRODUCTION

PRESENT day research in CMOS technology is largely geared toward improving MOSFETs performance and increasing device density through aggressive scaling of their feature sizes [1]. Quantum–mechanical size effects become important in nanoscale MOSFETs where the inversion layers are just a few nanometers thick. Meanwhile, the transistors are expected to operate in the quasi-ballistic transport regime as the channel length becomes comparable with the mean free path of the carriers in the inversion layer.

The injection velocity, which is the ballistic carrier velocity at the top of the barrier near the source, is the main driving force for improved transistor performance with scaling. It has been demonstrated [2], [3] that the drive current in the quasi-ballistic regime is mainly limited by the injection velocity. Moreover, multisubband Monte Carlo simulations [4] have confirmed the significant impact on performance of an increase of injection velocity. It has been reported recently that the carrier mobility

is closely correlated with the carrier velocity [5]. This parameter is thus a key figure of merit of devices operating in the quasi-ballistic regime, so an understanding of how the ballistic injection velocity is related to band structure is important in understanding device physics and assessing performance limits.

The ballistic limit for device performance has been extensively explored for double-gate MOSFETs with Si, Ge, and alternative channel materials and various surface/transport orientations [6]–[10]. Effective mass models with bulk transport and confinement effective masses are assumed in these models. As devices scale down to a few nanometers thick, however, the continued use of bulk effective masses may not be adequate [11]. Nonparabolicity, which shifts the subband energy levels and changes the in-plane effective masses, becomes important for ultrathin-body (UTB) Si. By adopting a 20-band $sp^3 d^5 s^*$ -SO semiempirical atomistic tight-binding (TB) model with a self-consistent Poisson solver, we explore, in this paper, the nonparabolic band structure effects on the ballistic performance of a Si UTB double-gate transistor, and compare the results with the bulk effective mass approximation (EMA). In contrast to a recent study of similar issues [11], we use an TB treatment of the electronic structure, perform electrostatically self-consistent simulations, and compute device-relevant metrics such as ballistic injection velocity and ON-current. Our results support the conclusions of [11] that the parabolic EMA is an adequate first-order approximation for Si. We, however, find that the differences are large enough to merit attention.

This paper is organized as follows. Section II describes the TB approach and illustrates the nonparabolicity in the calculated band structure for a Si UTB. In Section III, we first calculate the ballistic injection velocities for different body thicknesses and various surface/transport orientations from the TB energy dispersion relation, and then, discuss and compare the results with those from the parabolic effective mass approach. Section IV summarizes the key findings of this paper.

II. APPROACH

The model device simulated in this paper is as shown in Fig. 1. The transport, transverse, and wafer orientations are along X -, Y -, and Z -axes, respectively. The band structure of such a thin film is calculated according to the TB approach, where 20 orbitals, consisting of an $sp^3 d^5 s^*$ basis with spin-orbit coupling, are used to represent each atom along the body thickness in the UTB Hamiltonian [12]–[14]. The TB coupling parameters we use are from [15], which have been optimized to accurately reproduce the bandgap and effective masses of bulk Si. At the Si surfaces, a hard wall boundary condition for the wavefunction is applied,

Manuscript received August 13, 2007; revised November 26, 2007. This work was supported by the MARCO MSD Focus Center. The review of this paper was arranged by Editor H. Jaouen.

The authors are with the School of Electrical and Computer Engineering, Purdue University, West Lafayette, IN 47907 USA (e-mail: liuy@purdue.edu; neophyto@purdue.edu; tlow@purdue.edu; gecko@purdue.edu; lundstro@purdue.edu).

Color versions of one or more of the figures in this paper are available online at <http://ieeexplore.ieee.org>.

Digital Object Identifier 10.1109/TED.2007.915056

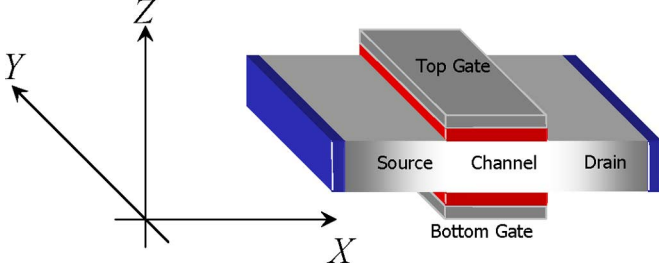


Fig. 1. Double-gate, ultrathin-body (UTB) device structure simulated. The transport, width, and wafer orientations are along X -, Y -, and Z -axes, respectively.

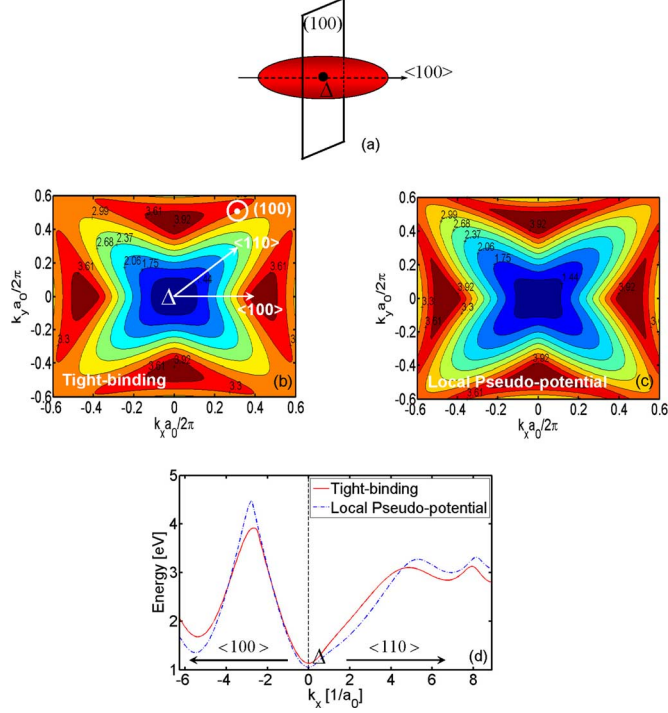


Fig. 2. Band structure calculated for bulk Si at Δ point: (a) in the plane of (100) , (b), (c), and (d) along $\langle 100 \rangle$ and $\langle 110 \rangle$ with the TB and local pseudopotential (PP) methods.

and the dangling bonds at the surfaces are passivated using a hydrogen-like termination model of the sp^3 hybridized interface atoms. This technique has been shown to successfully remove all the surface states from the bandgap [16].

The TB bulk band structure at the Δ point in the (100) plane [see Fig. 2(a)] is shown first in Fig. 2(b). Fig. 2(c) shows the result calculated by using an empirical local pseudopotential methods (EPM) [17]. In both plots, very similar starfruit-like nonparabolic energy contour at high energy levels are observed and show qualitative match. Fig. 2(d) shows the bulk $E-k$ dispersion along $\langle 100 \rangle$ and $\langle 110 \rangle$ orientations with both methods for comparison.

To explore the in-plane effective mass of an UTB, we first calculated the band structure of the thin film with infinitely high barriers (hard wall boundary conditions) at $V_G = 0$. We extracted the effective mass by fitting the dispersion to a parabolic one. We make sure that the parabolic $E-k$ gives the best fit to the TB dispersion up to $3k_B T$. Actually, the parabolic dispersion

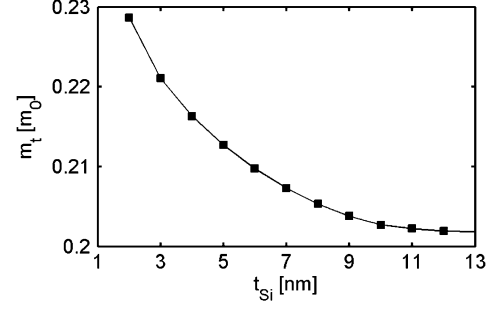


Fig. 3. In-plane effective mass m_t for the twofold valleys increases up to 10% higher than bulk value when the UTB body thickness (t_{Si}) is ≤ 3 nm.

can fit the TB one with high accuracy to even larger energy ranges. Fig. 3 shows the change of the in-plane effective mass in $(100)/\langle 100 \rangle$ orientation as the thin film thickness (t_{Si}) is reduced. For film thickness below about 3 nm, m_t for $(100)/\langle 100 \rangle$ is about 10% larger than the bulk value ($m_{t,bulk} = 0.20 m_0$). In [11], this effect was not observed, which suggests that the difference in various treatment of bandstructure may be significant from a device perspective. Fig. 4(a) plots the 2-D density-of-states for $t_{Si} = 3$ nm (23 atomic layers). The results are similar to [11], Fig. 9(a) and show that for high energies, the parabolic EMA is poor. For real devices, however, only the lowest few subbands are occupied. Fig. 4(b) plots the 2-D density-of-states for $t_{Si} = 3$ nm on a smaller energy scale that is relevant to the energy range that controls the ballistic injection velocity. Here, both the nonparabolicity of the twofold unprimed valleys and the subband energy level change are observed with respect to the bulk effective mass model. These effects get smaller as the body thickness increases. Note that the initial very small step for the first and second subbands of the twofold unprimed valleys is due to the valley splitting [18], which is also observed in [11]. Fig. 4(c) plots the 2-D density-of-states for $t_{Si} = 6$ nm (45 atomic layers) and less difference from bulk effective mass model is observed. These two factors (the change in energy levels or confinement effective mass and the change in the in-plane effective mass) combined together will lead to a difference in the current and injection velocity compared with the bulk EMA.

III. RESULTS AND DISCUSSION

In this section, the Si UTB n-MOSFET band structure is first calculated self-consistently by coupling the TB model and the Poisson equation. Then, the ballistic $I-V$ characteristic is calculated using a semiclassical FET model based on the TB $E-k$ relations and parabolic energy bands. The main features of the ballistic FET model [2], [19] are illustrated in Fig. 5, where the net current and inversion charge density are calculated from the band structure at the top of the barrier. Specifically, the group velocity of each state is calculated from the tabulated TB $E-k$ data of the UTB, and the carrier density is then evaluated by assuming that the states with a positive (negative) group velocity are in equilibrium with the source (drain) reservoir. The drain-current is then readily obtained by taking the difference between the source and drain fluxes, and the inversion charge is

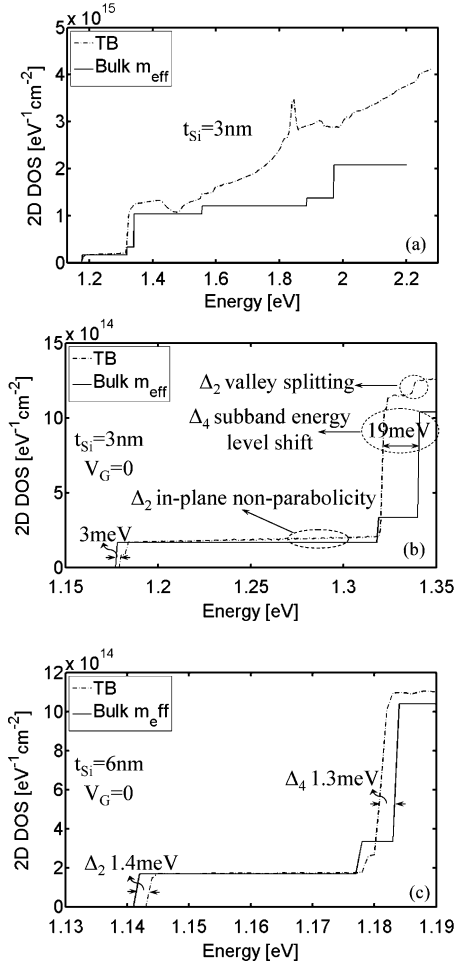


Fig. 4. Density-of-states. (a) $t_{Si} = 3$ nm. (b) $t_{Si} = 3$ nm. (c) $t_{Si} = 6$ nm. The lower and higher steps represent the Δ_2 and Δ_4 valleys, respectively. The nonparabolicity including both the change of the in-plane effective mass and the shift in subband energy levels is more prominent in the thinner body thickness UTB.

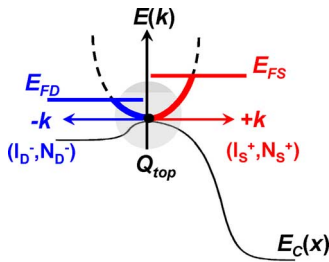


Fig. 5. Illustration of the essential aspects of the semiclassical ballistic FET model. The $E_C(x)$ curve represents the lowest electron subband in the device.

determined by summing up the carriers injected from the source and drain. The same self-consistent simulation procedures are applied with parabolic energy bands for the EMA, and the results are compared.

The symmetric, double-gate intrinsic UTB n-MOSFET device simulated has an equivalent oxide thickness (EOT) = 0.5 nm. Fig. 6 compares the inversion charge density, ballistic current, and injection velocity for (100)/(100) calculated from the TB model with that obtained from the bulk EMA for a body

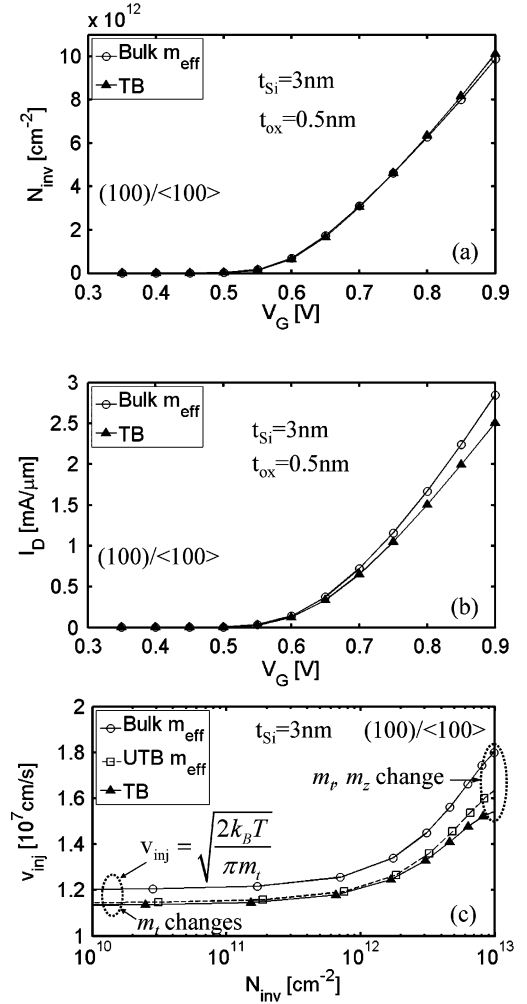


Fig. 6. Self-consistent results of the (a) charge density, (b) current, and (c) ballistic injection velocity for (100)/(100) UTB with $t_{Si} = 3$ nm, calculated by the TB model and bulk EMA. The charge matches well for these two methods. The current and injection velocity differs due to the change of the in-plane effective mass and shift in the subband energy level.

thickness $t_{Si} = 3$ nm at $V_D = 1$ V. The bulk effective masses used in this paper are $m_t = 0.89m_0$ and $m_l = 0.20m_0$, which are the target values of the TB parameters [15]. Fig. 6(a) shows that the inversion charge densities calculated by the TB and effective mass model are very close, since the charge is mainly controlled by electrostatics. In Fig. 6(b) and (c), a difference in the current and ballistic injection velocity between the TB and effective mass approach is observed. These differences are caused by two factors: firstly, in the nondegenerate limit, the injection velocity is related to the twofold valley in-plane effective mass m_t as $v_{inj} = \sqrt{2k_B T / \pi m_t}$ [2]. As discussed in Section II, m_t increases to $0.22m_0$ for $t_{Si} = 3$ nm due to the nonparabolicity of the bulk band structure. In Fig. 6(c), the injection velocity is recalculated with an adjusted $m_t = 0.22m_0$ and plotted in circles, and it matches well with the TB in the nondegenerate range. The injection velocity and current mismatch under strong inversion is due to the lowered subband energy level for the heavier fourfold primed valleys compared with bulk effective mass model. Fig. 7 clearly shows these two effects in the

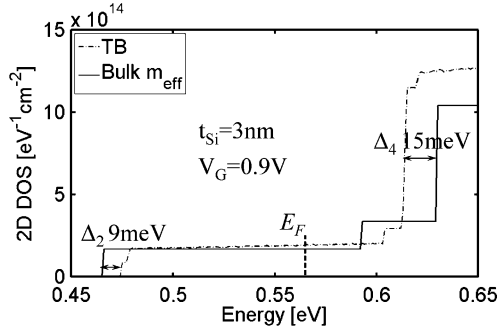


Fig. 7. Density-of-states plot for the UTB with $t_{Si} = 3$ nm at deep inversion. The change in confinement mass, increase of the in-plane mass, and in-plane nonparabolicity account for the difference in injection velocity as calculated by the two band structure models.

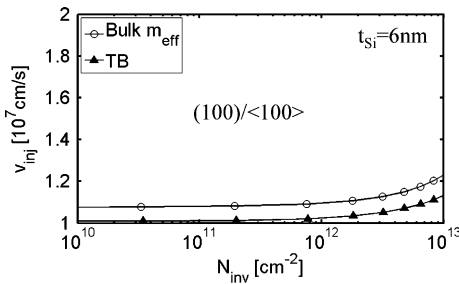


Fig. 8. Ballistic injection velocity calculated with the TB and bulk EMA for the UTB with $t_{Si} = 6$ nm plotted in the same scale as of Fig. 6(c) for comparison.

density-of-states plot at $V_G = 0.9$ V. The heavier fourfold valleys in the TB are about 14 meV lower than those of the bulk effective model. These two factors combined together result in the injection velocity and drain-current difference between the TB and bulk EMA. The difference of $\sim 15\%$ is not insignificant. Also note that the bandstructure model of [11] would likely produce even larger differences. Device researchers should be aware of the fact that various band structure models may produce significantly different predictions of the ballistic injection velocity.

The same device was simulated with a thicker body thickness of $t_{Si} = 6$ nm, and v_{inj} is shown in Fig. 8. The TB and bulk EMA give closer results due to the reduced importance of nonparabolicity for the thicker t_{Si} . There is also a significant decrease in v_{inj} compared with $t_{Si} = 3$ nm. This occurs because with a thicker body, the energy separation between the light twofold unprimed valleys and the heavy fourfold primed valleys becomes smaller; the heavier valleys are, therefore, important in carriers transport. Fig. 9 shows the density-of-states for $t_{Si} = 6$ nm at deep inversion where $N_{inv} = 1.03 \times 10^{13}/\text{cm}^2$ by both the TB and EMA. The nonparabolicity effects (both the in-plane m_t and the subband energy level change) are smaller, meanwhile the Fermi level is closer to the heavy valleys, leading to the decrease of v_{inj} . Fig. 10(a) and (b) plots the carrier occupancies for the twofold valleys and fourfold valleys with $t_{Si} = 3$ nm and $t_{Si} = 6$ nm, respectively. It is seen that the heavier fourfold valleys are lightly occupied for $t_{Si} = 3$ nm, but their occupancy is about 50% for $t_{Si} = 6$ nm, which decreases the injection velocity substantially.

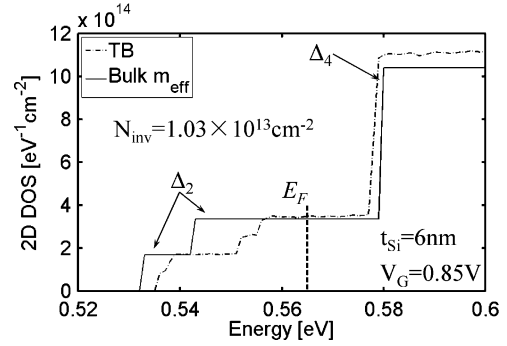


Fig. 9. Density-of-states for $t_{Si} = 6$ nm at deep inversion. The energy separation between the heavy and light valleys is smaller with thicker body thickness, leading to decrease in injection velocity.

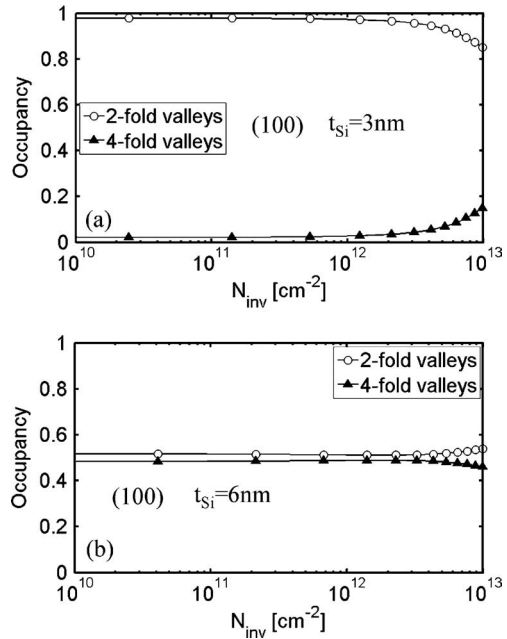


Fig. 10. Charge occupancy of the twofold and fourfold valleys. (a) $t_{Si} = 3$ nm. (b) $t_{Si} = 6$ nm. For $t_{Si} = 3$ nm, most of the carriers are transported through the twofold valleys, while for $t_{Si} = 6$ nm, the heavier fourfold valleys are as important as the twofold valleys, leading to decreased injection velocity.

Next, the empirical TB model was generalized to treat arbitrary confinement and transport orientations with self-consistency for an UTB. The injection velocities for different orientations were calculated and compared with effective mass model. The intrinsic device has the same EOT = 0.5 nm. For comparison with the effective mass model, the transport, width, and confinement effective masses for different crystal orientations were obtained as explained in [20] and [21]. Table I lists the effective masses used for all orientations in this paper.

The injection velocities for different wafer/transport orientations were calculated and are shown in Fig. 11(a) with TB, and in Fig. 11(b), with bulk EMA for $t_{Si} = 6$ nm. Both plots indicate that (100)/(110) is the best and (110)/(110) is the worst for v_{inj} of the Si UTB n-MOSFET. Note that the injection velocity in (100)/(110) orientation is larger than in (100)/(100) orientation; this is because the fourfold primed valleys are also important in

TABLE I
TRANSPORT, WIDTH, AND CONFINEMENT EFFECTIVE MASSES AND SUBBAND
DEGENERACIES OF Si FOR THE FIVE DIFFERENT ORIENTATIONS STUDIED

(wafer)/[transport] /[width]	m_x	m_y	m_z	Deg.
(001)/[100]/[010]	m_l	m_l	m_l	2
	m_t	m_t	m_t	2
	m_l	m_t	m_t	2
(001)/[110]/[1 $\bar{1}$ 0]	m_l	m_t	m_l	2
	$2m_t m_l / (m_t + m_l)$	$(m_t + m_l) / 2$	m_t	4
(110)/[001]/[1 $\bar{1}$ 0]	m_l	m_t	m_t	2
	m_t	$(m_t + m_l) / 2$	$2m_t m_l / (m_t + m_l)$	4
(110)/[1 $\bar{1}$ 0]/[001]	m_l	m_t	m_t	2
	$(m_t + m_l) / 2$	m_t	$2m_t m_l / (m_t + m_l)$	4
(111)/[11 $\bar{2}$]/[1 $\bar{1}$ 0]	$(m_t + 2m_l) / 3$	m_t	$3m_t m_l / (m_t + 2m_l)$	2
	$2m_t [(m_t + 2m_l) / (m_t + m_l)] / 3$	$(m_t + m_l) / 2$	$3m_t m_l / (m_t + 2m_l)$	4

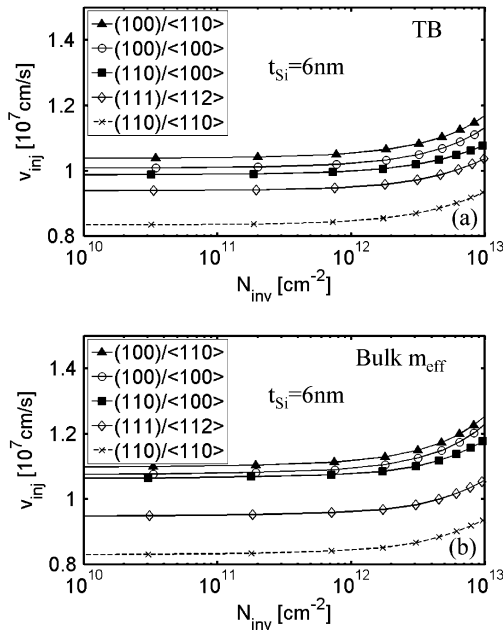


Fig. 11. Ballistic injection velocity for different crystal orientations calculated. (a) TB. (b) Bulk EMA. The injection velocity follows the same trend of measured mobility data of different orientations.

conducting carriers when $t_{Si} = 6$ nm. Furthermore, it is interesting to note that the injection velocity follows the same trend as the experimental data for the carrier mobility for different orientations [22], and we surmise that there is a close correlation between the two physical parameters [5]. These results suggest that the ballistic injection velocity is a useful metric in both the ballistic, quasi-ballistic, and diffusive regimes.

IV. CONCLUSION

By using an $sp^3d^5s^*$ -SO TB approach, we explored, in this paper, nonparabolicity effects and examined the validity of the parabolic EMA for ballistic transport in the UTB Si n-MOSFETs. In argument with [11], we found that the simple, widely used parabolic bulk EMA is reasonably accurate for the UTB Si structures. It is, however, important to realize that effective masses generally increase as the body thickness decreases. It is also important to note that different band structure models in current use give different quantitative predictions. For the TB model here, the use of bulk effective masses overesti-

mates the injection velocity by about 10%–20% as compared with the TB results. The injection velocity was also found to be highly dependent on device structure, specially the body thickness. Finally, both the TB and EMAs for the injection velocity show the same trend as the experimental data for the mobility as a function of surface/transport orientation, indicating a close correlation between them.

ACKNOWLEDGMENT

The computational resources for this research were provided through nanoHUB.org by the Network for Computational Nanotechnology.

REFERENCES

- [1] ITRS Public Home Page. (2005). [Online]. Available: <http://www.itrs.net/Common/2005ITRS/Home2005.htm>.
- [2] K. Natori, "Ballistic metal-oxide-semiconductor field effect transistor," *J. Appl. Phys.*, vol. 76, no. 8, pp. 4879–4890, 1994.
- [3] M. Lundstrom, "Device physics at the scaling limit: What matters?," in *IEDM Tech. Dig.*, 2003, pp. 789–792.
- [4] L. Lucci, P. Palestri, D. Esseni, and L. Selmi, "Multi-subband Monte Carlo modeling of nano-MOSFETs with strong vertical quantization and electron gas degeneration," in *IEDM Tech. Dig.*, 2005, pp. 617–620.
- [5] A. Khakifirooz and D. A. Antoniadis, "Transistor performance scaling: The role of virtual source velocity and its mobility dependence," in *IEDM Tech. Dig.*, 2006, pp. 667–670.
- [6] F. Assad, Z. Ren, D. Vasileska, S. Datta, and M. Lundstrom, "On the performance limits for Si MOSFETs: A theoretical study," *IEEE Trans. Electron Devices*, vol. 47, no. 1, pp. 232–240, Jan. 2000.
- [7] T. Low, Y. T. Hou, M. F. Li, C. Zhu, A. Chin, G. Samudra, L. Chan, and D.-L. Kwong, "Investigation of performance limits of germanium double-gated MOSFETs," in *IEDM Tech. Dig.*, 2003, pp. 691–694.
- [8] S. E. Laux, "Simulation study of Ge n-channel 7.5 nm DGFETs of arbitrary crystallographic alignment," in *IEDM Tech. Dig.*, 2004, pp. 135–138.
- [9] A. Pethe, T. Krishnamohan, D. Kim, S. Oh, H.-S. P. Wong, Y. Nishi, and K. C. Saraswat, "Investigation of the performance limits of III–V double-gate n-MOSFETs," in *IEDM Tech. Dig.*, 2005, pp. 605–608.
- [10] M. D. Michielis, D. Esseni, and F. Diussi, "Analytical models for the insight into the use of alternative channel materials in ballistic nano-MOSFETs," *IEEE Trans. Electron Devices*, vol. 54, no. 1, pp. 115–123, Jan. 2007.
- [11] J. L. Van Der Steen, D. Esseni, P. Palestri, L. Selmi, and R. J. E. Huetting, "Validity of the parabolic effective mass approximation in silicon and germanium n-MOSFETs with different crystal orientations," *IEEE Trans. Electron Devices*, vol. 54, no. 8, pp. 1843–1851, Aug. 2007.
- [12] J. M. Jancu, R. Scholz, F. Beltram, and F. Bassani, "Empirical $sp^3d^5s^*$ tight-binding calculation for cubic semiconductors: General method and material parameters," *Phys. Rev. B*, vol. 57, pp. 6493–6507, 1998.
- [13] G. Klimeck, R. C. Bowen, T. B. Boykin, C. Salazar-Lazaro, T. A. Cwik, and A. Stoica, "Si tight-binding parameters from genetic algorithm fitting," *Superlattices Microstruct.*, vol. 27, pp. 77–88, 2000.
- [14] T. B. Boykin, G. Klimeck, R. C. Bowen, and F. Oyafuso, "Diagonal parameter shifts due to nearest-neighbor displacements in empirical tight-binding theory," *Phys. Rev. B*, vol. 66, pp. 125207–125212, 2002.
- [15] T. B. Boykin, G. Klimeck, and F. Oyafuso, "Valence band effective-mass expressions in the $sp^3d^5s^*$ empirical tight-binding model applied to a Si and Ge parameterization," *Phys. Rev. B*, vol. 69, pp. 115201–115210, 2004.
- [16] S. Lee, F. Oyafuso, P. von Allmen, and G. Klimeck, "Boundary conditions for the electronic structure of finite-extent embedded semiconductor nanostructures," *Phys. Rev. B*, vol. 69, pp. 045316–045323, 2004.
- [17] M. L. Cohen and T. K. Bergstresser, "Band structures and pseudopotential form factors for fourteen semiconductors of the diamond and zinc-blende structures," *Phys. Rev.*, vol. 141, pp. 789–796, 1966.
- [18] A. Rahman, G. Klimeck, M. S. Lundstrom, T. B. Boykin, and N. Vagidov, "Atomic approach for nanoscale devices at the scaling limit and beyond—Valley splitting in Si," *Jpn. J. Appl. Phys.*, vol. 44, no. 4B, pp. 2187–2190, 2005.
- [19] A. Rahman, J. Guo, S. Datta, and M. S. Lundstrom, "Theory of ballistic nanotransistors," *IEEE Trans. Electron Devices*, vol. 50, no. 9, pp. 1853–1864, 2003.

- [20] A. Rahman, M. S. Lundstrom, and A. W. Ghosh, "Generalized effective-mass approach for n-type metal-oxide-semiconductor field-effect transistors on arbitrarily orientated wafers," *J. Appl. Phys.*, vol. 97, pp. 053702–053713, 2005.
- [21] F. Stern and W. E. Howard, "Properties of semiconductor surface inversion layers in the electric quantum limit," *Phys. Rev.*, vol. 163, no. 3, pp. 816–835, 1967.
- [22] M. Yang, V. W. C. Chan, K. K. Chan, L. Shi, D. M. Fried, J. H. Stathis, A. I. Chou, E. Gusev, J. A. Ott, L. E. Burns, M. V. Fischetti, and M. Jeong, "Hybrid-orientation technology (HOT): Opportunities and challenges," *IEEE Trans. Electron Devices*, vol. 53, no. 5, pp. 965–978, May 2006.



Yang Liu (S'05) received the B.S. degree in applied physics in 2003 from the University of Science and Technology of China, Hefei, China, and the M.S. degree in mechanical engineering in 2005 from Purdue University, West Lafayette, IN, where he is currently working toward the Ph.D. degree in the School of Electrical and Computer Engineering.

His current research interests include modeling quantum transport in nanoscale devices, bandstructure effects on the performance of nano MOSFETs in Si as well as new channel materials and structures.



Neophytos Neophytou (S'05) received the B.S. degree in electrical and computer engineering in 2001 and the M.S. degree in microelectronics and nanotechnology in 2003 from Purdue University, West Lafayette, IN, where he is currently working toward the Ph.D. degree.

His current research interests include computational modeling of quantum–mechanical electron transport through carbon nanotubes, nanowires, graphene-based channels, new channel materials, effects of bandstructure on the electronic properties of

nanowires as well as the effect of atomistic variations and defects in the transport on nanoscale devices.



Tony Low (S'05) received the Ph.D. degree in electrical engineering from the National University of Singapore, Singapore, in 2007.

He is currently a Postdoctoral Fellow at Purdue University, West Lafayette, IN, where he is engaged in research on modeling of spin-based transistors, graphene devices, and ab-initio-based semiempirical bandstructure methods.



Gerhard Klimeck (S'94–M'96–SM'04) received the German Elect. Eng. degree from Ruhr-University Bochum, Bochum, Germany, in 1990, and the Ph.D. degree from Purdue University, West Lafayette, IN, in 1994.

He is currently an Associate Director of technology in the Network for Computational Nanotechnology and a Professor of electrical and computer engineering at Purdue University. He leads the development and deployment of Web-based simulation tools (<http://nanohub.org>). He was the Technical Group Supervisor of the Applied Cluster Computing Technologies Group. He is also a Part-Time Principal Member at the NASA Jet Propulsion Laboratory. He was a member of technical staff at the Central Research Laboratory, Texas Instruments. He is the author or coauthor of over 180 peer-reviewed publications and over 310 conference presentations. His current research interests include modeling of nanoelectronic devices, parallel cluster computing, and genetic algorithms. He has been the lead in the development of nanoelectronic modeling (NEMO) 3-D, a tool that enables the simulation of tens-of-million atom quantum dot systems, and NEMO 1-D, the first nanoelectronic computer-aided design (CAD) tool.

Prof. Klimeck is a member of the American Physical Society (APS), the Eta Kappa Nu (HKN), and the Tau Beta Pi (TBP).



Mark S. Lundstrom (S'72–M'74–SM'80–F'94) received the B.E.E. and M.S.E.E. degrees from the University of Minnesota, Minneapolis, in 1973 and 1974, and the Ph.D. degree in electrical engineering from Purdue University, West Lafayette, IN, in 1980.

From 1974 to 1977, he was with Hewlett-Packard Corporation, Loveland, CO, where he was engaged in research on integrated circuit process development and manufacturing support. In 1980, he joined the School of Electrical Engineering, Purdue University, where he is currently the Don and Carol Scifres Distinguished Professor of electrical and computer engineering and the Founding Director of the Network for Computational Nanotechnology. From 1989 to 1993, he was the Director of the Optoelectronics Research Center, Purdue University, where from 1991 to 1994, he was an Assistant Dean of engineering. His current research interests include the physics of small electronic devices, especially nanoscale transistors and on carrier transport in semiconductor devices.

Prof. Lundstrom is currently the Distinguished Lecturer of the IEEE Electron Device Society. He is a Fellow of the American Physical Society and the American Association for the Advancement of Science. He was the recipient of the Frederick Emmons Terman Award from the American Society for Engineering Education in 1992, the Semiconductor Research Corporation's Technical Excellence Award in 2002, the Semiconductor Industry Association's University Researcher Award for his career contributions to the physics and simulation of semiconductor devices in 2005, and the IEEE Electron Devices Society's Education Award in 2006. He is also a corecipient of the 2002 IEEE Cleo Brunetti Award for the work on nanoscale electronic devices.

Prof. Lundstrom is currently the Distinguished Lecturer of the IEEE Electron Device Society. He is a Fellow of the American Physical Society and the American Association for the Advancement of Science. He was the recipient of the Frederick Emmons Terman Award from the American Society for Engineering Education in 1992, the Semiconductor Research Corporation's Technical Excellence Award in 2002, the Semiconductor Industry Association's University Researcher Award for his career contributions to the physics and simulation of semiconductor devices in 2005, and the IEEE Electron Devices Society's Education Award in 2006. He is also a corecipient of the 2002 IEEE Cleo Brunetti Award for the work on nanoscale electronic devices.